



# Suspended LRSPP for the development of highly integrated active plasmonic devices

M. A. FUENTES-FUENTES,<sup>1</sup> D. A. MAY-ARRIOJA,<sup>2,\*</sup> J. R. GUZMAN-SEPULVEDA,<sup>3</sup> F. ARTEAGA-SIERRA,<sup>4</sup> M. TORRES-CISNEROS,<sup>2,5</sup> P. L. LIKAMWA,<sup>3</sup> AND J. J. SÁNCHEZ-MONDRAGÓN<sup>1</sup>

<sup>1</sup>Photonics and Optical Physics Laboratory, Optics Department, INAOE, Puebla, Puebla 72000, México

<sup>2</sup>Centro de Investigaciones en Óptica, Prol. Constitución 607, Fracc. Reserva Loma Bonita, Aguascalientes 20200, México

<sup>3</sup>CREOL, The College of Optics and Photonics, University of Central Florida, Orlando, FL 32816, USA

<sup>4</sup>The Institute of Optics, University of Rochester, Rochester, NY 14627, USA

<sup>5</sup>Applied Physics Group, DICIS, University of Guanajuato, Salamanca, Guanajuato 368850, México

\*darrioja@cio.mx

**Abstract:** We present a novel long-range surface plasmon polariton (LRSPP) device consisting of a suspended dielectric matrix in which an electrically active, millimeter-long metallic waveguide is embedded. We show that, by opening an air gap under the lower cladding, the influence of the substrate is suppressed and the symmetry of the thermo-optical distribution around the LRSPP waveguide is preserved over extended ranges of applied electrical current with minimal optical losses. Experimental results show that, compared to a standard nonsuspended structure, our device allows either the induction of a phase change that is three times larger, for a fixed electrical power, or, equivalently, a scaling down of the device to one-tenth of its original length, for a fixed phase change.

© 2019 Optical Society of America under the terms of the [OSA Open Access Publishing Agreement](#)

## 1. Introduction

The design of novel integrated photonics devices can involve many different approaches and configurations depending upon the requirements of specific applications. Nevertheless, in general, one typically targets maximizing the device's response, simplifying its structure, and minimizing its size. For these purposes, the use of surface plasmon polaritons (SPPs) can be a suitable option due to the inherently large sensitivity to external perturbations of light propagating along metal-dielectric interfaces. This property triggered the use of SPP, for instance, in sensing applications, with the first papers being reported shortly after the first demonstrations in 1983 [1] and reaching almost 400 papers per year just a few years later in 1997 [2]. SPPs are transverse magnetic (TM) polarized optical surface waves that propagate along a metal-dielectric interface. SPPs were described at the beginning of the past century [3] and experimentally reported in the late sixties [4,5]. Since then, they have been extensively studied and most of their properties have been assessed [6]. One of the most significant characteristics of SPPs is their associated short propagation distance which can reach about 19  $\mu\text{m}$  and 3  $\mu\text{m}$  in an air-silver and air-gold interface, respectively, at visible and near-infrared wavelengths [6]. This high attenuation is a consequence of the propagation along the single metal-dielectric interface which confines a fraction of the optical field into the metal, and thus this high attenuation is caused primarily by free-electron scattering in the metal. Nevertheless, the propagation distance can be increased by more than two orders of magnitude by reducing the thickness of the metal layer and embedding the metal stripe in dielectric matrix, i.e., by sandwiching the metal stripe between claddings with similar optical properties [7]. The symmetric plasmonic structure reduces the confinement of the propagating mode, which in turns reduces the overlap with the metal stripe and the attenuation is significantly reduced. This kind of SPP is known as long-range SPP (LRSPP) since its

characteristic propagation length is significantly longer as compared to SPP. Although reduced confinement can be an issue in some applications, the improved propagation length opens the door for a mirage of application for LRSPP.

To date, the vast majority of applications based on LRSPP deal with devices containing passive structures [8–11], such as straight waveguides, S-bends, Y-junction splitters, and Mach-Zehnder interferometers (MZI), among others [8,11,12]. However, there are specific applications where having the ability to change the amplitude and/or phase of the propagating optical signal through devices like interferometers, switches, or modulators, is critical. In the case of LRSPP, active devices can be easily achieved by adding contacts to the metal stripe and then applying an electrical current to the contacts [13]. For the case of a metal stripe embedded into a polymer matrix, this would allow the entire metal stripe to be heated up and, due to the large thermo-optic effects involved, appreciable effective refractive index (RI) changes can be induced. Using similar principles, different configurations for active LRSPP devices have been proposed and demonstrated for MZIs [14–16], directional coupler switches [14], variable attenuators [17–20] and tunable bandpass filters [21,22].

A critical limitation in the above-mentioned scenarios is the existence of a small range for the applied electrical current, i.e., in the case of active devices requiring pure phase changes, there exists an electrical current threshold after which the insertion losses of the LRSPP begin to increase and eventually become very large. This is due to the fact that the heat dissipation is not uniform between the bottom dielectric/substrate interface and the top dielectric/air interface. This anisotropic heat dissipation effectively results in an asymmetric temperature distribution in the bottom and top dielectric layers which, in turn, induces a difference in the effective RI of the claddings due to the thermo-optic effect of the dielectric matrix. Such RI difference will induce several effects such as mode distortion and radiation losses, as well as a conversion from a long-range regime to short-range, which will gradually attenuate the transmitted signal as the applied electrical current is increased [23,24]. In order to achieve appreciable phase changes while maintaining a long-range operation, one could attempt to use longer active regions over which the cumulative effects would be similar. Unfortunately, this would require active devices with significantly larger dimensions, which is not desirable not just because an important objective of photonic integration is the optimization of the use of wafer real estate, but also because longer devices will be more susceptible to adverse effects caused by the presence of surface defects.

In this work, we present a new device structure configuration for LRSPP which consists of a suspended active region achieved by removing material from the interface between the bottom cladding and the substrate. This approach allows having the top and bottom claddings with similar heat dissipation properties and, effectively therefore, with more symmetric temperature distributions. This, in turn, helps to minimize the RI difference between the two claddings, when an electrical current is applied to the metallic waveguide and the temperature is increased. This permits LRSPP operation over an extended range of values of electrical current and at the same time maintaining shorter device length requirements. Our approach is rather general and can be extended to sensing platforms in which the waveguide itself is the sensing element [25] or it can be incorporated into more complex active architectures, e.g., arms of interferometers [26,27]. In this particular work, we first show, both numerically and experimentally, that the suspended structure in the integrated device works as symmetric LRSPP device over an extended range of electric currents, as compared to a traditional (non-suspended) structure with the same dimensions. Next, we experimentally demonstrate the use of this concept by embedding the device in one arm of a free space MZI, to show that significantly large phase changes can be induced while maintaining negligible attenuation, as opposed to the non-suspended structure. In section 2, we discuss the principles of operation for the proposed structure, and the hypothesis is well supported by our numerical results. In section 3, we explain, in detail, the microfabrication of the samples. In section 4, we describe

the experiment and present the results that were obtained using the fabricated devices. Finally, in section 5, we present our conclusion of the present work.

## 2. Principle of operation

As mentioned previously, our approach is to incorporate a simple geometry in the design of the devices that leads to symmetric heat dissipation around the active region of the integrated LRSPP waveguide, and the devices can be realized experimentally with standard photolithography techniques and in academic-grade cleanrooms. For this endeavor, we propose a simple idea: reducing the strong influence of the substrate by detaching it from the bottom cladding, at least underneath the active region. This will permit a more symmetric heat dissipation above and below the LRSPP waveguide. In order to verify our scheme, we implemented a set of numerical simulations using COMSOL Multiphysics.

Firstly, we studied numerically a symmetric structure, where the metal stripe is embedded in a polymer matrix, i.e., same material for the top and bottom claddings, and the whole structure supported on a silicon wafer, as illustrated in Fig. 1(a). From the literature, we can select typical values for the width of the metal stripe and the thickness of the polymer claddings [9,10,28–31], leaving the thickness of the metal stripe as the only parameter to minimize attenuation. In this baseline simulation, we chose the thickness of the polymer matrix as 20  $\mu\text{m}$ , i.e., 10 $\mu\text{m}$ -thick claddings, with the waveguide centered both horizontally and vertically within this matrix. For the claddings material, we have selected SU-8, which is a standard photoresist used in lithography-based microfabrication [32,33]. The RI of the SU-8 and gold used in the simulations are  $\eta_{\text{SU-8}} = 1.57 + 0i$  [34] and  $\eta_g = 0.55 + 11.4912i$  [35], respectively, for free-space wavelength operating at  $\lambda_0 = 1.55 \mu\text{m}$ . Using this data in our numerical simulations, we verify that the plasmonic waveguide embedded in the polymer matrix indeed supports a propagating optical mode. Given that the SU-8 claddings are thick enough, a rapid verification can be done by simulating only the metallic waveguide embedded into the polymer matrix without taking into account the other layers in the structure i.e., without the substrate [see Fig. 1(a)]. Figure 1(b) shows the real and imaginary part of the effective RI of the supported mode as a function of the thickness of the metal stripe for a fixed width of  $w = 5 \mu\text{m}$ . As expected, the guided mode is only supported for TM polarization. Moreover, from the imaginary part of the mode index, it can be seen that the thickness of the metal film needs to be  $< 20 \text{ nm}$ , for this particular width of the waveguide, so as not to incur large insertion losses. In the subsequent simulations, the thickness of the metal layer has been set to  $t = 15 \text{ nm}$ .

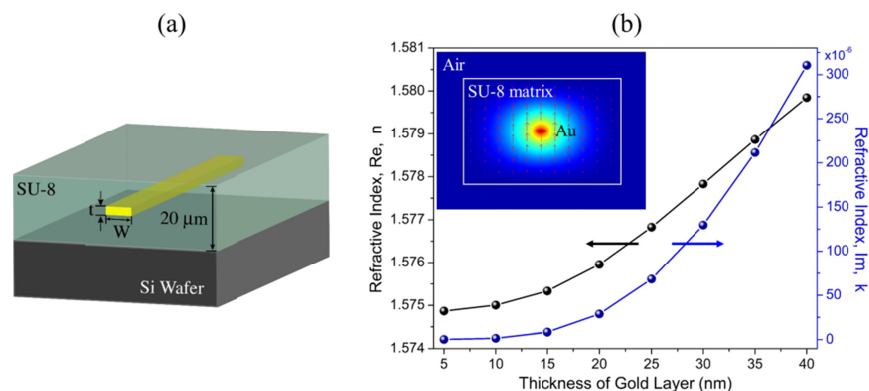


Fig. 1. (a) LRSPP consisting of an Au stripe embedded in a SU-8 polymer matrix. (b) Complex effective RI obtained numerically by varying the stripe Gold thickness ( $t$ ).

The cross-sectional temperature distributions in the two structures: the traditional, non-suspended structure [see Fig. 2(a)], and our proposed suspended one [see Fig. 2(b)] are

numerically simulated to assess the influence of the substrate on the symmetry of the temperature distribution. Recall that an asymmetric temperature distribution will, in turn, produce a difference in the effective RI of the claddings that can take the plasmonic waveguide to a short-range regime. The simulation of the temperature distribution was performed by introducing the presence of an electrical current flowing along the metal stripe and in the same direction of the optical propagation. In this way, heat flows from the metal stripe outwards and the asymmetry of the temperature distribution in close proximity to the metal stripe can be evaluated. When the electrical current is applied to the metal stripe, the Joule effect is present and the heat from the waveguide is dissipated into the SU-8 matrix. Simulations of Joule heating and thermal transfer were performed using the Heat Transfer module from COMSOL Multiphysics. The change of the RI by the SU-8 thermo-optic effect is given by  $n(\Delta T) = n_0 + \alpha \Delta T$ , where  $n_0$  is the RI at room temperature,  $\alpha$  is the thermo-optic coefficient (TOC), and  $\Delta T$  is the change of temperature caused by the thermal transfer. As a boundary condition, natural convection is established by the convective heat flux physics.

We consider a 5 $\mu\text{m}$ -wide gold film, the thermal conductivity and the heat capacity of the SU-8 polymer are 0.3  $W/(m\cdot K)$  [36] and 1200  $J/(Kg\cdot K)$  [37], respectively. The whole structure sits on top of a 500 $\mu\text{m}$ -thick silicon wafer with a top layer of 5  $\mu\text{m}$  thick silicon dioxide, as shown in Fig. 2(a). In the simulation, we also consider that the electrical current is flowing into the page. Figure 2(c) shows the cross-sectional temperature distribution in the non-suspended LRSPP (NS-LRSPP) structure, for four different values of applied electrical current (4, 5, 6 and 7 mA), as indicated. From these color maps, the asymmetry of the temperature distribution due to the presence of the substrate is evident. Another perspective is shown in Fig. 2(d), in which vertical cuts of the color maps in Fig. 2(c) (at the center of the metal stripe) are plotted. It can be seen that both the temperature in the metal layer and its temperature difference with respect to the edges of the SU-8 layer (at  $-10\ \mu\text{m}$  and  $+10\ \mu\text{m}$ ), increase with increasing electrical current. This difference of temperature between the boundaries of the SU-8 matrix could reach 3.0  $\pm$  0.5  $^\circ\text{C}$  and consequently the corresponding RI difference in the two extremes of the SU-8 layer oscillate around  $5.61 \times 10^{-4}$  (SU-8 TOC =  $-1.87 \times 10^{-4}\ ^\circ\text{C}^{-1}$ ) [38]. Therefore, we can notice that even for very low electrical currents the RI difference can easily reach values of  $5 \times 10^{-4}$ , which is a typical value of the threshold tolerance for defining the long-range operation, i.e., if the index difference is  $>5 \times 10^{-4}$  the operation is considered short-range [23]. This means that active NS-LRSPP devices require longer LRSPP waveguides to apply very low electrical currents.

In order to compare the effect of our proposed structure, we perform the same numerical analysis for the suspended LRSPP structure (S-LRSPP). The suspended structure is fabricated by opening an air gap underneath the embedded waveguide such that the lower cladding resembles the thermal properties of the top cladding (air), as shown in Fig. 2(b). In this way, the effective heat dissipation properties of the bottom cladding will be similar to those from the top cladding. We emphasize that the approach followed here allows for a simple fabrication process without the need of additional steps that may include, for instance, the deposition of more layers i.e., polymer matrix sandwiched between sets of layers that allow thermal isolation from the substrate and have, effectively, similar heat dissipation properties.

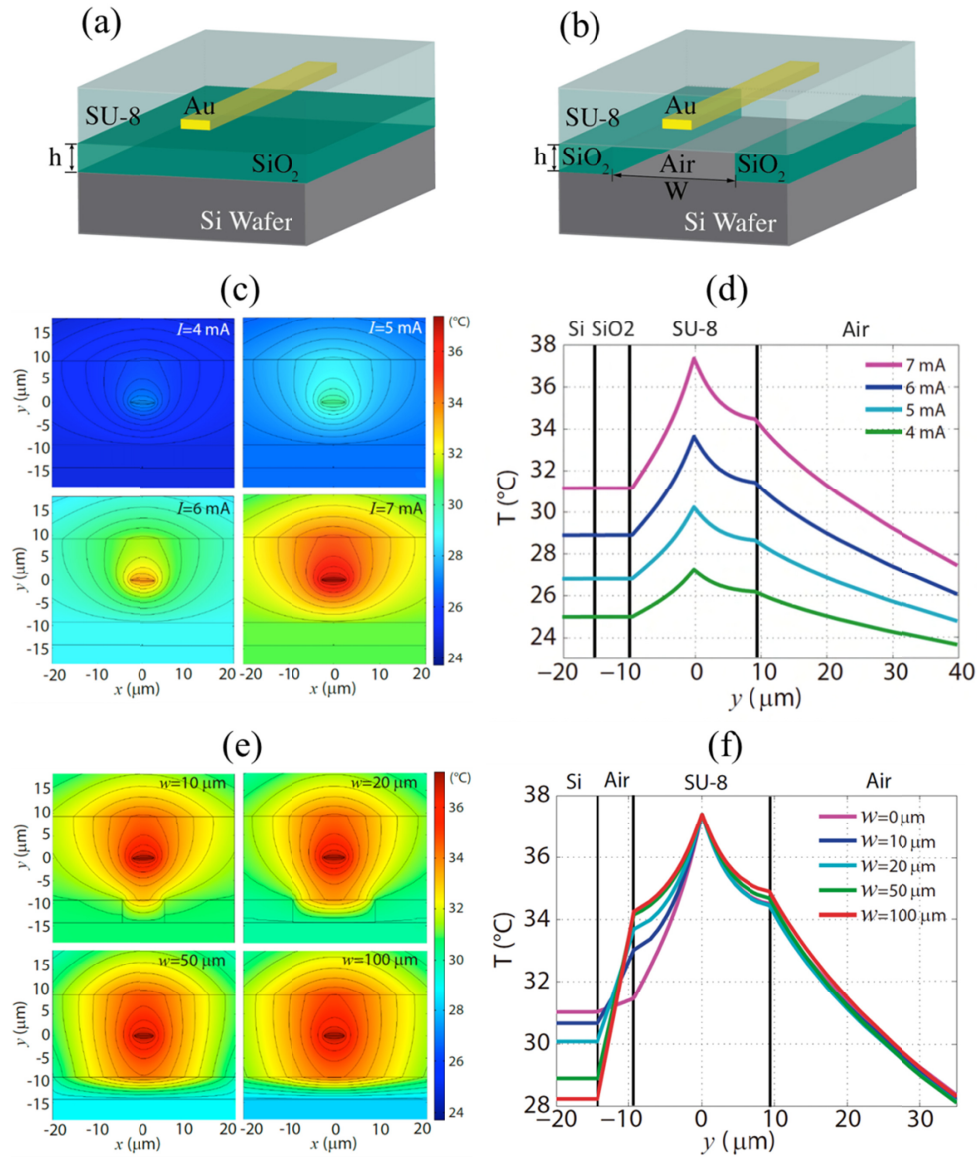


Fig. 2. Schematic of (a) the NS-LRSPP structure, and (b) the S-LRSPP structure. (c) Cross-sectional temperature distribution for different values of electrical current (4, 5, 6 and 7 mA) for the NS-LRSPP, and (d) the corresponding vertical cuts at the center of the waveguide. (e) Cross-sectional temperature distribution for a S-LRSPP with air gaps of different width ( $W = 10, 20, 50$  and  $100$  μm), with  $h = 5$  μm and  $I = 7$  mA, and (f) the corresponding vertical cuts at the center of the waveguide.

Figure 2(e) shows the cross-sectional temperature distributions of the S-LRSPP structure for different widths of the air gap underneath the polymer matrix as indicated in the panels. The current circulating along the metal stripe is 7 mA and is kept constant such that the only free parameter is the width of the air gap. From these color maps, it can be seen that the asymmetry of the temperature distribution decreases as we increase the width of the air gap, as expected for the top and bottom claddings that approach similar heat dissipation characteristics. From the vertical cuts at the center of the metal stripe, the reduction of the asymmetry can be verified [see Fig. 2(f)]. Moreover, we can corroborate that for a width of

the air gap of 50  $\mu\text{m}$  (green line) the temperature difference between the two edges of the SU-8 layer, is less than  $1^\circ\text{C}$ . Finally, it can also be seen that, for a given thickness of the air gap (5  $\mu\text{m}$  in our case, as determined by the layer of  $\text{SiO}_2$ ), there exists a maximum width of the gap after which the temperature distribution cannot be made more symmetric. In our example, this can be seen from the fact that similar temperature distribution is achieved in the vicinity of the waveguide even when the width of the gap is doubled from 50  $\mu\text{m}$  to 100  $\mu\text{m}$ .

### 3. LRSPP device fabrication

Both the S-LRSPP and the NS-LRSPP were fabricated on the same wafer sample in order to avoid differences during their fabrication and provide a direct comparison in their performance. The main steps in the fabrication process are schematically illustrated in Fig. 3. The sample was prepared on a  $12 \times 10 \text{ mm}^2$  silicon substrate from which the native oxide was first removed using buffered oxide etching (BOE) and then thoroughly rinsed (sequentially) with deionized (DI) water, acetone, methanol, and isopropanol.

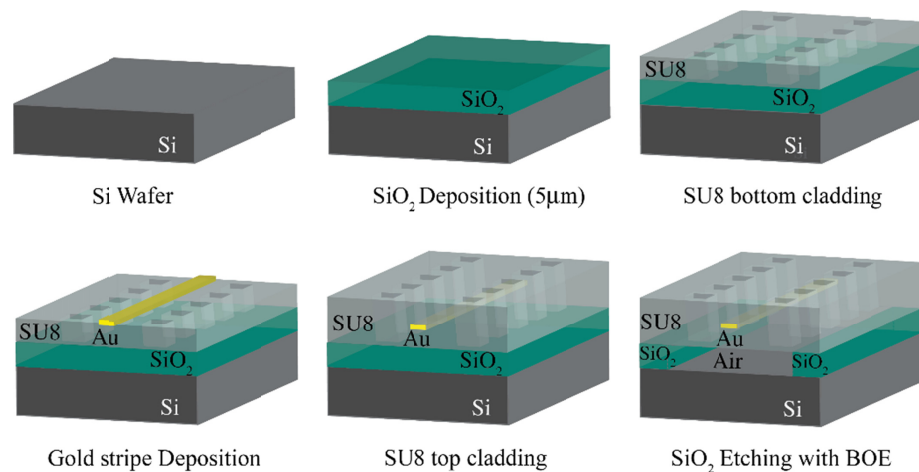


Fig. 3. A schematic overview of the main steps required in the fabrication of the suspended LRSPP devices.

Immediately after cleaning a silicon substrate material, a 5  $\mu\text{m}$ -thick layer of silicon dioxide ( $\text{SiO}_2$ ) was deposited by means of plasma-enhanced chemical vapor deposition (PECVD; Plasma-Therm 790 Series), at a rate of 49-50 nm/min for a total duration of the deposition process of 100 min. This layer of  $\text{SiO}_2$  will be removed at the end of the process in order to suspend the LRSPP. Nevertheless, subsequent fabrication steps after  $\text{SiO}_2$  deposition require improving the surface adhesion of this layer to ensure that the device (SU-8 matrix) remains attached to the substrate during fabrication. The surface adhesion was enhanced by inducing some roughness via oxygen plasma etching (plasma descum). This process was performed for 1 min duration only to avoid excessive roughness or damaging the  $\text{SiO}_2$  layer.

The bottom cladding of the LRSPP device was prepared (on top of the layer of  $\text{SiO}_2$ ) by spin-coating, non-diluted SU-8 3010 polymer from Micro-chem Soft at 3500 rpm during 40 s for a thickness of the SU-8 layer of 10  $\mu\text{m}$ . The sample was baked at  $95^\circ\text{C}$  for a duration of 7 min and then exposed to UV light for 12 s at an incident power of  $12 \text{ mW/cm}^2$ . This photolithography process was performed using a Karl Suss UV Mask Aligner to expose and delineate a mask containing square windows that would be used to open the holes that will allow chemical etchant access to the  $\text{SiO}_2$  layer later on [see Fig. 3]. After exposing with UV light, the sample was soft baked at  $95^\circ\text{C}$  for a duration of 3 min for the release of thermal stress and the non-cured polymer was revealed by immersing the sample into the standard SU-8 developer for 1.5 min. Finally, in order to ensure the integrity of the substrate throughout the rest of the fabrication process, the SU-8 cladding was fully cured by hard

baking the sample in a step-like fashion from 100 °C to 200 °C in increments of 25 °C every minute.

The next step is the fabrication of the gold stripes. Again, to improve the surface adhesion, a 1 min oxygen plasma etching was performed. We then applied NR9-1000 PY negative photoresist from Futurrex on the SU-8 bottom cladding, by spin-coating at 4000 rpm for 40 s to obtain a final thickness of 1  $\mu\text{m}$ . The sample was soft baked at 150 °C for 1 min and then exposed to UV light for 18 s at an incident power density of 12  $\text{mW}/\text{cm}^2$  using the proper mask to delineate the metal stripe waveguides. After the UV exposure, the sample was baked at 100 °C for 1 min and the channels were revealed by immersing the sample into RD-6 resist developer for 11 s. Once the channels for the waveguides were open, Cr (1 nm)/Au (15 nm)/Cr (1 nm) were sequentially deposited by thermal evaporation (Edwards Auto 306 with quartz crystal thickness monitor). The bottom chromium layer is needed to improve adhesion of the gold layer and the top chromium layer is deposited to maintain the symmetry of the metal layers. Both the width of the resist channels and the thickness of the metal films were carefully monitored to avoid introducing additional losses in the device. After the metal evaporation, a standard lift-off process was used to remove the remaining metal on top of the negative photoresist while leaving only the metallic waveguides.

In similar fashion to the bottom cladding, the upper cladding was fabricated by spin-coating undiluted SU-8 3010 at 3500 rpm for 40 s to obtain a thickness of 10  $\mu\text{m}$ . This layer was also baked at 95 °C for 7 min and then exposed to UV light for 12 s at an incident power of 12  $\text{mW}/\text{cm}^2$ . The same mask containing the square windows was used when exposing the upper cladding to UV light for opening the access holes through the entire thickness of the device (20  $\mu\text{m}$ -thick polymer matrix). After UV exposure, the sample was baked at 95 °C for 3 min and the uncured polymer was revealed using standard SU-8 developer (1.5 min immersion). Similarly to the bottom cladding, the SU-8 upper cladding was fully cured by hard baking the sample in a step-like fashion from 100 °C to 200 °C in increments of 25 °C every minute. Recalling how sensitive the plasmonic waveguides are to asymmetries in the RI distribution, it is worth mentioning that this last hard baking on the top cladding is important to balance the properties (both mechanical and optical) of the bottom and top cladding.

Finally, the LRSPP was isolated from the substrate by removing the portion of the sacrificial layer of SiO<sub>2</sub> that is underneath the waveguide via wet chemical etching by immersing the sample in a 6:1 Buffered Oxide Etch (BOE) solution for a duration of 45 min. to form the suspended waveguide structure. The schematic cross-section of the final suspended SU-8/Au/SU-8 structure can be seen in the last panel of Fig. 3. We should also note that for the case of the NS-LRSPP structure the square holes are not defined besides the metal stripes and thus the BOE etching does not affect these structures at all. It is also important to mention that the schematic diagrams shown in Fig. 3 (specially the last panel) are not drawn to scale and that the holes opened to access the SiO<sub>2</sub> layer are significantly far away from the lateral end (edge) of the metal stripe. In other words, it means that there is sufficient polymer besides the metal stripe such that the medium can be assumed to be infinite in the lateral direction.

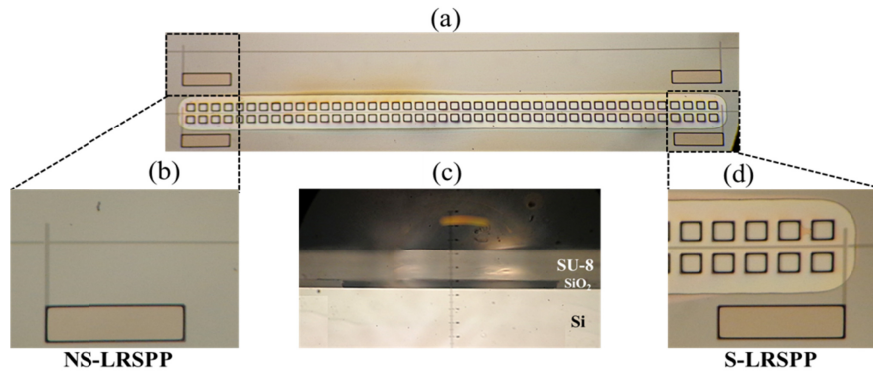


Fig. 4. (a) Top view picture of the fabricated LRSP devices showing both the NS-LRSPP and the S-LRSPP structures. (b) The zoom shows the NS-LRSPP structure in more detail, where the Au stripe is connected to the Au contact. (c) The picture shows a cross section of the S-LRSPP structure with the suspended SU8 layer. (d) The zoom shows the S-LRSPP structure in detail, where we see the small square windows used to etch the SiO<sub>2</sub> below the SU8 and the Au stripe running between the squares and connected to the Au contact.

A digital photograph of the fabricated sample (top view) is shown in Fig. 4(a). As shown in Fig. 4(a), each batch consists of pairs of NS-LRSPP (top horizontal line) and S-LRSPP waveguides (bottom horizontal line surrounded by small squares) in order to guarantee that the LRSP physical dimensions are the same for both kinds of structures. In Fig. 4(b), the zoomed region shows the NS-LRSPP waveguide which is connected to the gold contacts at the ends of the waveguides. The zoomed region in Fig. 4(d) shows more clearly the S-LRSPP waveguide that runs in between the small square holes and is also connected to gold contacts. Finally, a cross sectional view of the S-LRSPP structure is shown in Fig. 4(c), where the suspended SU8 layer can be observed.

#### 4. Experiments and results

In order to test the performance of the fabricated devices, we perform both transmission and interferometric experiments with the setup shown schematically in Fig. 5 (labeled as experiment A and B, respectively). In both experiments, the contacts at the ends of the waveguide [see Fig. 4(a)] were connected to electrodes and electrical current was passed through the metal waveguide. This allows us to use the waveguide as the heat source and produce an outwards heat flow, from the waveguide core to the claddings, in order to induce a RI change via the thermo-optic effect induced in the claddings. After the LRSP structure is heated, it will reach thermal equilibrium and the temperature distribution will exhibit a degree of asymmetry that will be dependent on the LRSP structure employed, i.e. non-suspended vs suspended. As the temperature distribution becomes asymmetric the RI distribution becomes asymmetric as well, and the insertion losses of the LRSP waveguide are significantly increased. Therefore, by measuring the propagation losses (transmission) we can infer the degree of temperature asymmetry of the plasmonic waveguide structure. The induced phase change of the LRSP waveguide can be measured using a standard free-space MZI.

The two experiments (transmission and interferometric) can be carried out using the same setup by simply removing or placing the mirror M3. The transmission experiment i.e., Experiment A, enclosed by the black segmented line, is performed by removing the Mirror M3, which allows the beam coming from the second microscope objective to reach beam splitter BS3, and split the beam to measure the optical power and record the LRSP mode distribution simultaneously. The interferometric experiment i.e., Experiment B, enclosed by the blue segmented line, is achieved by leaving the Mirror M3 at the position shown in Fig. 5. This allows the beam going through the sample and the beam going through the variable optical attenuator (VOA) to reach beam splitter BS2 and interfere at the IR camera.

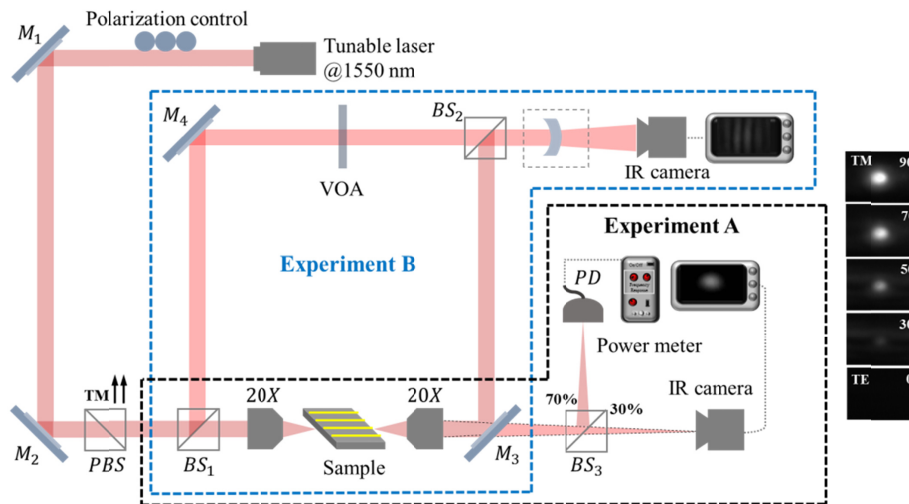


Fig. 5. Experimental setup for measuring the optical power transmitted and phase changes through the NS-LRSPP and S-LRSPP waveguides. The images shown to the right are the power transmitted at different polarizations with  $\lambda = 1.55 \mu\text{m}$ , stripe width of  $5 \mu\text{m}$  and  $15 \text{nm}$  thick.

The tunable laser (Hewlett Packard model 8164A) was fixed at a wavelength of  $1550 \text{ nm}$  and full polarization control was implemented to ensure having only TM polarized light. The light was coupled into and out of the sample using  $20\times$  microscope objective lens. The output beam was then split into two beams (70/30 split ratio) for simultaneous measurement of the transmitted optical power and for imaging of the output intensity distribution. The optical power was measured with an infrared photodetector (Newport 918D-IR-OD3) and a power meter (Newport 1916-C), and the output intensity distribution was imaged onto an infrared vidicon camera (Electrophysics Micron Viewer model 7290A).

As a baseline sanity check, the fabricated samples were tested to verify that they were only able to support the TM polarized mode. The right vertical row in Fig. 5 shows the intensity distribution at the output of the waveguide imaged onto the CCD for different polarizations. From this point on, the polarization was kept fixed as TM.

The transmitted intensity at the fixed wavelength of  $1550 \text{ nm}$ , for both the NS-LRSPP and S-LRSPP structures, was measured as a function of the electrical current flowing through the waveguide. Measurements were first performed by systematically increasing the electrical current until we obtained almost complete attenuation in the non-suspended waveguide. At each electrical current value the electrical resistance was measured until a maximum applied electrical power of  $70 \text{ mW}$  is obtained, which corresponds to a maximum measured resistance of  $11.3 \text{ k}\Omega$ . The suspended waveguide was measured by increasing the electrical current until we reach the same maximum electrical power, which corresponds to a maximum measured electrical resistance of  $5.8 \text{ k}\Omega$ . This allowed us to have a direct comparison between the two LRSPP structures. The maximum electrical current was  $2.5 \text{ mA}$  and  $3.5 \text{ mA}$  for the NS-LRSPP and S-LRSPP waveguides, respectively, which corresponds to a maximum electrical power of  $70 \text{ mW}$ . In both cases, the electrical current was increased at a constant rate of  $0.25 \text{ mA/min}$ . In both LRSPP structures, the waveguide has a width of  $5 \mu\text{m}$  with a total length of  $5 \text{ mm}$ , where the active length is  $4 \text{ mm}$ .

Figure 6(a) shows a direct comparison between the transmitted optical power through the NS-LRSPP and S-LRSPP waveguide as a function of the applied electrical power. We can observe that both structures exhibit total insertion losses of  $\sim 8 \text{ dB}$ , including input/output end-fire coupling losses, which is in agreement with similar works [10,14,18]. We can also observe that the NS-LRSPP structure rapidly exhibits higher losses for an electrical power

beyond 13 mW. This corresponds to different effects such as mode distortion and radiation losses, as well as a transition from long to short range SPP due to asymmetric heat dissipation. Nevertheless, in the case of the S-LRSPP structure, we can observe that losses only start to appear for electrical powers beyond 46 mW and furthermore the loss increment is rather slow. We can also notice some mild rises and drops at the beginning of the S-LRSPP curve, which we believe are related to the fact that the RI close to the metal becomes lower compared to its surrounding, and thus the optical field is less confined in the metal which reduces the ohmic losses. Ultimately, losses will dominate and the intensity is reduced.

It can be also noted that, by taking as reference the net attenuation experienced in the S-LRSPP waveguide (from  $-8$  dB to  $-15$  dB in the entire range from 0 to 70 mW), as compared to the NS-LRSPP (from  $-8$  dB to  $-15$  dB only in the first 22 mW), the incorporation of the air gap is enough to extend the range of operation about three times while maintaining low insertion losses.

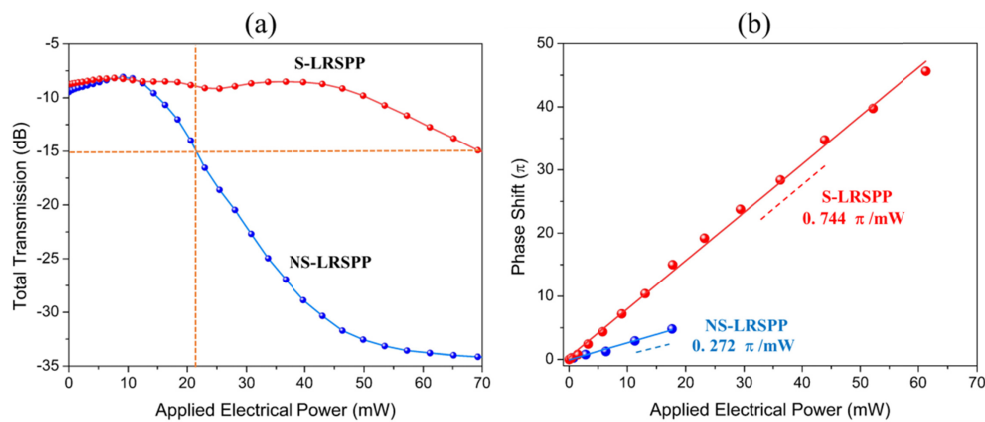


Fig. 6. Experimental results obtained for the NS-LRSPP and S-LRSPP devices. a) Comparison of the total power transmitted as a function of the applied electrical power. b) Comparison of phase shift response as a function of the applied electric power.

The fact that losses are reduced in the S-LRSPP structure means that by increasing the applied electrical power, a larger phase change can be achieved with negligible impact to the LRSPP propagation. This should allow us to reduce the length of the active LRSPP structure while still achieving sufficient phase changes. The phase change introduced by the LRSPP structures was measured interferometrically by placing the device in one arm of a MZI, as shown schematically in Fig. 5 (Experiment B). Again, 20X microscope objective lenses are used to couple light into and out of the waveguide under test and two 50/50 beam splitters are used at the input and output of the MZI. A variable attenuator is used in the arm without waveguide in order to compensate for the insertion losses from the LRSPP waveguide end-fire coupling setup and hence optimize the contrast of the interference pattern. The interference pattern, i.e. fringes, was projected onto the camera and recorded for further processing and analysis as the applied electrical power is increased.

Figure 6(b) shows the net phase shift, in units of  $\pi$ , for both LRSPP structures. In both cases, a linear dependence of the phase shift on the applied electrical power was obtained. It is evident that in the case of the non-suspended waveguide structure, the maximum tolerable applied power is lower as this is related to the reduced visibility of the fringes as the electrical power is increased. As expected, the insertion losses are higher for the NS-LRSPP structure, which limits the electrical power range where the phase change can be measured. This experiment was carried out using the same pair of NS-LRSPP and S-LRSPP waveguides used in the prior experiment. It is also important to mention that we are measuring the total phase change induced through the LRSPP waveguides. Although the change in the effective RI is

determined mainly by the large negative value of the TOC of the polymer matrix, other effects such as the phase introduced by the flowing electrons influence the overall response [39].

More interestingly, the experiments show that the linear responses of the NS-LRSPP and S-LRSPP structures have different slopes. This reveals a second aspect of the asymmetric structure that can be understood in terms of an effective TOC exhibited by the overall structure combined with a large thermal conductivity from the Si substrate of  $148 \text{ W/m}\cdot\text{K}$ . In the case of the S-LRSPP waveguide, the TOC of the SU-8 ( $-1.87 \times 10^{-4} \text{ }^\circ\text{C}^{-1}$  [38]) mostly determines the temperature response of the device as the polymer matrix is considered to be somewhat isolated from the substrate. In addition, since the top and bottom claddings are surrounded by air, the net heat dissipation from the polymer is reduced due to the small thermal conductivity from the air of  $0.026 \text{ W/m}\cdot\text{K}$  and heat dissipation via convection. However, in the case of the NS-LRSPP structure the presence of a solid conductive substrate consisting of materials with positive TOC,  $1 \times 10^{-5} \text{ }^\circ\text{C}^{-1}$  and  $1.8 \times 10^{-4} \text{ }^\circ\text{C}^{-1}$  for  $\text{SiO}_2$  and Si, respectively [18], can decrease the thermally induced phase shift.

This is an interesting feature that allows accessing the underlying interplay between the geometry of the structure and the properties of the materials involved. On the one hand the temperature distribution is changed to a more symmetric configuration by isolating the LRSPP from the substrate at the expense of having a stronger temperature dependence; on the other hand, the temperature dependence can be significantly reduced with a substrate with large thermal conductivity combined with a proper waveguide design to allow enough overlap of the mode with substrate having a TOC of opposite sign to that of the matrix in which the waveguide is embedded at the expense of sacrificing the symmetry of the RI distribution. This can be used to optimize the performance of the LRSPP for other applications by finding the proper balance between the symmetry and the side effects from both the architecture and the material's properties standpoint.

We should also highlight that the response time of the S-LRSPP is expected to be slower than the NS-LRSPP owing to the lack of thermal conductivity in the suspended structure. Nevertheless, it may be feasible to enhance the response time by modifying the S-LRSPP while maintaining the operational RI symmetry.

As a final remark, if we set a maximum 'acceptable' attenuation to be  $-11 \text{ dB}$ , as indicated in Fig. 6(a), we can observe that this threshold value is reached for an electrical power of about  $15 \text{ mW}$  for the NS-LRSPP structure and about  $55 \text{ mW}$  for the S-LRSPP. Since the slopes of the induced phase change are linear, as shown in Fig. 6(b), we can consider a figure of merit of  $0.06875 \text{ } \pi/\text{mW}\cdot\text{mm}$  and  $0.191 \text{ } \pi/\text{mW}\cdot\text{mm}$ , for the NS-LRSPP and S-LRSPP, respectively, for an active LRSPP waveguide of  $4 \text{ mm}$  in length. Using the electric powers of  $15 \text{ mW}$  and  $55 \text{ mW}$ , respectively, for the slopes of the phase changes, we find that in  $1 \text{ mm}$  of propagation, it is possible to have a phase change of about  $\pi$  for the NS-LRSPP structure while, for the same length, the phase change in the S-LRSPP is about  $10\pi$ . Equivalently, this means that we can obtain a phase change of about  $\pi$  in  $1 \text{ mm}$  of propagation for the traditional structure or in  $0.1 \text{ mm}$  of propagation in the suspended device. This represents a scale-down factor of one order of magnitude in the required length of the LRSPP waveguide. Based on this result, one can anticipate a two-fold advantage of the proposed suspended structure: on one hand, for active LRSPP-based devices, higher integrability can be possible with waveguides that are ten times shorter; on the other hand, for LRSPP-based sensors, one order of magnitude enhancement in the sensor's sensitivity can be achieved.

## 5. Conclusions

In conclusion, we have numerically and experimentally demonstrated that the inherent losses in active LRSPP plasmonic waveguides, which are mainly due to the asymmetric distribution of temperature in the top and bottom claddings imposed by the strong influence of the semiconductor substrate, can be significantly reduced by suspending the active region. We

have demonstrated such a suspended polymer-embedded plasmonic waveguide by etching a sacrificial layer ( $\text{SiO}_2$ ) from the interface between the bottom cladding and the substrate. This approach effectively removes the strong dependence on the thermal properties of the substrate and permits having similar heat dissipation properties above and below the waveguide, which results in a more symmetric temperature distribution around the waveguide over an extended range of applied electrical power. The result is that we can use higher values of electrical power in the S-LRSPP structure while minimizing the insertion losses. This allows us to use shorter lengths of S-LRSPP structure and still obtain large enough phase changes. In the experiments, we have compared side by side our proposed suspended structure with the conventional non-suspended one. Experimental results demonstrate that the suspended structure can operate at electrical powers which are 3 times larger than the maximum that can be held by the conventional structure. Additionally, the phase change rate for the suspended structure was measured to be 2.8 times larger than that obtained for the conventional structures. In other words, we have demonstrated that by using suspended structures, the fabrication of devices operating based on thermally induced phase changes can be scaled down almost 3 times when we use the same value of electric power. However, the most important result of this work is that since the suspended structure allows us to use more electric power, it means that we can obtain the same phase change with a waveguide length that is just 10% of the length of a non-suspended structure.

### Funding

Consejo Nacional de Ciencia y Tecnología (CB2016-286368, CB2016-286629, CB2008-01-101378, and graduates scholarship and internship no. 348374); Universidad de Guanajuato (CIIC 72/2018); Secretaría de Educación Pública (511-6/17-7051).

### Acknowledgments

Project CB2008-01-101378 was selected among the success cases by CONACyT at the “CASOS DE ÉXITO Y REPENSANDO LA EVALUACIÓN CIENTÍFICA” past administration program closure event.

### Disclosures

The authors declare that there are no conflicts of interest related to this article.

### References

1. B. Liedberg, C. Nylander, and I. Lundström, “Surface plasmon resonance for gas detection and biosensing,” *Sens. Actuators* **4**, 299–304 (1983).
2. J. Homola, S. S. Yee, and G. Gauglitz, “Surface plasmon resonance sensors: review,” *Sens. Actuators B Chem.* **54**(1-2), 3–15 (1999).
3. R. W. Wood, “On a remarkable case of uneven distribution of light in a diffraction grating spectrum,” *Proc. Phys. Soc. Lond.* **18**(1), 269–275 (1902).
4. E. Kretschmann and H. Raether, “Radiative decay of non-radiative surface plasmons excited by light,” *Z. Naturforsch. B* **23**(12), 2135–2136 (1968).
5. A. Otto, “Excitation of nonradiative surface plasma waves in silver by the method of frustrated total reflection,” *Zeitschrift für Phys.* **216**(4), 398–410 (1968).
6. A. D. Boardman, *Electromagnetic Surface Modes* (Wiley, 1982).
7. D. Sarid, “Long-range surface-plasma waves on very thin metal films,” *Phys. Rev. Lett.* **47**(26), 1927–1930 (1981).
8. R. Charbonneau, “Demonstration of a passive integrated optics technology based on plasmons,” University of Ottawa (2001).
9. A. Boltasseva, “Integrated-optics components utilizing long-range surface plasmon polaritons,” Technical University of Denmark (2004).
10. A. Boltasseva, T. Nikolajsen, K. Leosson, K. Kjaer, M. S. Larsen, and S. I. Bozhevolnyi, “Integrated optical components utilizing long-range surface plasmon polaritons,” *J. Lightwave Technol.* **23**(1), 413–422 (2005).
11. R. Charbonneau, N. Lahoud, G. Mattiussi, and P. Berini, “Demonstration of integrated optics elements based on long-ranging surface plasmon polaritons,” *Opt. Express* **13**(3), 977–984 (2005).
12. R. Charbonneau, C. Scales, I. Breukelaar, S. Fafard, N. Lahoud, G. Mattiussi, and P. Berini, “Passive integrated optics elements based on long ranging surface plasmon polaritons,” *J. Lightwave Technol.* **24**(1), 477–494

- (2006).
13. H. Fan, R. Charbonneau, and P. Berini, "Long-range surface plasmon triple-output Mach-Zehnder interferometers," *Opt. Express* **22**(4), 4006–4020 (2014).
  14. T. Nikolajsen, K. Leosson, and S. I. Bozhevolnyi, "Surface plasmon polariton based modulators and switches operating at telecom wavelengths," *Appl. Phys. Lett.* **85**(24), 5833–5835 (2004).
  15. H. Fan and B. Pierre, "Noise cancellation in long-range surface plasmon dual-output Mach-Zehnder interferometers," *J. Lightwave Technol.* **31**(15), 2606–2612 (2013).
  16. T. Liu, L. Ji, G. He, X. Sun, Y. Yi, X. Wang, C. Chen, F. Wang, and D. Zhang, "Transmission of long-range surface plasmon-polaritons across gap in Au waveguide," *J. Opt.* **18**(1), 015006 (2016).
  17. K. Leosson, T. Nikolajsen, A. Boltasseva, and S. I. Bozhevolnyi, "Long-range surface plasmon polariton nanowire waveguides for device applications," *Opt. Express* **14**(1), 314–319 (2006).
  18. G. Gagnon, N. Lahoud, G. Mattiussi, and P. Berini, "Thermally activated variable attenuation of long-range surface plasmon-polariton waves," *J. Lightwave Technol.* **24**(11), 4391–4402 (2006).
  19. J. Tang, Y. R. Liu, L. J. Zhang, X. C. Fu, X. M. Xue, G. Qian, N. Zhao, and T. Zhang, "Flexible thermo-optic variable attenuator based on long-range surface plasmon-polariton waveguides," *Micromachines (Basel)* **9**(8), 369 (2018).
  20. X. Sun, Y. Xie, T. Liu, C. Chen, F. Wang, and D. Zhang, "Variable optical attenuator based on long-range surface plasmon polariton multimode interference coupler," *J. Nanomater.* **2014**, 1–9 (2014).
  21. J. Lee, F. Lu, and M. A. Belkin, "Broadly wavelength tunable bandpass filters based on long-range surface plasmon polaritons," *Opt. Lett.* **36**, 3744–3746 (2011).
  22. J. Lee and M. A. Belkin, "Widely tunable thermo-optic plasmonic bandpass filter," *Appl. Phys. Lett.* **103**(18), 181115 (2013).
  23. I. Breukelaar and P. Berini, "Long-range surface plasmon polariton mode cutoff and radiation in slab waveguides," *J. Opt. Soc. Am. A* **23**(8), 1971–1977 (2006).
  24. S. Park, M. S. Kim, J. J. Ju, J. T. Kim, S. K. Park, J. M. Lee, W. J. Lee, and M. H. Lee, "Temperature dependence of symmetric and asymmetric structured Au stripe waveguides," *Opt. Commun.* **283**(17), 3267–3270 (2010).
  25. O. Krupin, W. R. Wong, F. R. Mahamd Adikan, and P. Berini, "Detection of small molecules using long-range surface plasmon polariton waveguides," *IEEE J. Sel. Top. Quantum Electron.* **23**(2), 103–112 (2017).
  26. H. Fan and P. Berini, "Bulk sensing using a long-range surface-plasmon dual-output Mach-Zehnder interferometer," *J. Lightwave Technol.* **34**(11), 2631–2638 (2016).
  27. H. Fan and P. Berini, "Bulk sensing using a long-range surface-plasmon triple-output Mach-Zehnder interferometer," *J. Opt. Soc. Am. B* **33**(6), 1068–1074 (2016).
  28. P. Berini, "Plasmon-polariton waves guided by thin lossy metal films of finite width: Bound modes of asymmetric structures," *Phys. Rev. B Condens. Matter Mater. Phys.* **63**(12), 125417 (2001).
  29. P. Berini, "Optical waveguide structures," U.S. patent 6,741,782 (2004).
  30. T. Nikolajsen, K. Leosson, I. Salakhutdinov, and S. I. Bozhevolnyi, "Polymer-based surface-plasmon-polariton stripe waveguides at telecommunication wavelengths," *Appl. Phys. Lett.* **82**(5), 668–670 (2003).
  31. S. J. Al-Bader, "Optical transmission on metallic wires; fundamental modes," *IEEE J. Quantum Electron.* **40**(3), 325–329 (2004).
  32. K. K. Tung, W. H. Wong, and E. Y. B. Pun, "Polymeric optical waveguides using direct ultraviolet photolithography process," *Appl. Phys., A Mater. Sci. Process.* **80**(3), 621–626 (2005).
  33. Z. Ling and K. Lian, "In situ fabrication of SU-8 movable parts by using PAG-diluted SU-8 as the sacrificial layer," *Microsyst. Technol.* **13**(3-4), 253–257 (2007).
  34. J. M. Ruano-López, M. Aguirregabiria, M. Tijero, M. T. Arroyo, J. Elizalde, J. Berganzo, I. Aranburu, F. J. Blanco, and K. Mayora, "A new SU-8 process to integrate buried waveguides and sealed microchannels for a Lab-on-a-Chip," *Sens. Actuators B Chem.* **114**(1), 542–551 (2006).
  35. P. B. Johnson and R. W. Christy, "Optical constants of the noble metals," *Phys. Rev. B* **6**(12), 4370–4379 (1972).
  36. Microchem, "Processing guidelines for SU-8 2000 permanent epoxy negative photoresist," (Microchem, 2015).
  37. J. L. Lai, C. J. Liao, and G. D. J. Su, "Using an SU-8 photoresist structure and cytochrome C thin film sensing material for a microbolometer," *Sensors (Basel)* **12**(12), 16390–16403 (2012).
  38. X. Lin, T. Ling, H. Subbaraman, L. J. Guo, and R. T. Chen, "Printable thermo-optic polymer switches utilizing imprinting and ink-jet printing," *Opt. Express* **21**(2), 2110–2117 (2013).
  39. H. Fan and P. Berini, "Thermo-optic characterization of long-range surface-plasmon devices in Cytop," *Appl. Opt.* **52**(2), 162–170 (2013).